INTERNATIONAL JOURNAL FOR NUMERICAL METHODS IN FLUIDS
Int. J. Numer. Meth. Fluids 2009; **60**:827–845
Published online 9 September 2008 in Wiley InterScience (www.interscience.wiley.com). DOI: 10.1002/fld.1914

Optimized compact filtering schemes for computational aeroacoustics

Liu Zhanxin*,†, Huang Qibai, Hu Li and Yuan Jixuan

Department of Mechanical Engineering, Huazhong University of Science and Technology, Wuhan, Hubei 430074, People's Republic of China

SUMMARY

Spurious waves are inevitably introduced in the simulation of computational aeroacoustics problems by finite difference schemes. Filters are proposed to damp the spurious waves as soon as they are generated. A family of filtering schemes, both interior and boundary, are optimized in this paper. The transfer functions of the filters are approximated to modified Gaussian functions and sharp spectral cutoffs are obtained. The advanced sequential quadratic programming method is employed to get the approximation. Although all of the optimized filters are stable and perform well in the computation, we find that the optimized fourth-order filters are sufficient for different kinds of requirements. The improvements of the accuracy and convenient application of the optimized filters are demonstrated when applied to one- and two-dimensional problems. Copyright © 2008 John Wiley & Sons, Ltd.

Received 5 December 2007; Revised 6 May 2008; Accepted 29 July 2008

KEY WORDS: filtering schemes; compact schemes; optimization; finite difference; sequential quadratic programming; computational aeroacoustics

1. INTRODUCTION

Aeroacoustic problems usually involve sound waves of many octave bands. Several finite difference schemes [1–4] have been designed or optimized to resolve the waves with high accuracy and good spectral resolution. But the finite difference approximation invariably introduces numerical dispersion, dissipation errors and anisotropy. Spurious waves that include dispersive and parasite waves [5] are produced in several ways: (i) initial conditions; (ii) nonlinear cascade to small scales in direct numerical simulation (DNS) and large-eddy simulation (LES); (iii) shock waves and nonlinear steeping of waves; (iv) propagation of waves thorough grid stretching generalized

*Correspondence to: Liu Zhanxin, Department of Mechanical Engineering, Huazhong University of Science and Technology, Wuhan, Hubei 430074, People's Republic of China.
†E-mail: hustliuzx@gmail.com, liuzx1213@163.com

Contract/grant sponsor: National Natural Science Foundation of China; contract/grant number: 50075029

coordinates and overset grids; (v) boundary conditions [6]. When excessive amount of spurious waves are produced, they lead not only to the degradation of the quality of the numerical solution, but also to numerical instability. Thus it is necessary to use a filter or some other form of artificial dissipation to stabilize the solution. Because filter formulas are derived purely from spectral considerations with relatively little direct recourse to the governing equations being solved, filtering is viewed as a more versatile and general technique than damping [7].

Vichnevetsky and Alpert [8, 9] first introduced filtering to attenuate spurious waves in finite difference schemes. Such filters do not have a sharp spectral cutoff, but rather continuously vary from 1 to 0 over the range of wave numbers $0<kh<\pi/2$. Later, Lele [2] derived a set of compact filters that are superior to explicit formulas of the same stencil. Gaitonde and Younge [10] Visbal and Yaitonde [11] formulate a hierarchy of tridiagonal symmetric filters with different Taylor order accuracy. They applied the filters to simulate complex unsteady subsonic flows by incorporation with a five-point compact difference [12]. Subsequently many researchers derived near boundary filters [13–15] and applied the filters to DNS and LES [16–18]. Recently, Bogey and Bailly [19] optimized 11 and 13 points stencil explicit filters. Although the aforementioned tridiagonal and explicit filters perform well, they are large stencils which need more than 10 points to give a sharp spectral cutoff. What is more, it is time-consuming and laborious to choose a proper control variable of the filters in [13, 14]. What is more important is that the near boundary filtering schemes of Visbal and Gaitonde [13, 14] amplify the high wave number spurious and they cannot damp spurious waves in some wave number domains. This point will be discussed in detail in Section 3.

The present effort is to optimize Lele's [2] compact filters for computational aeroacoustics (CAA). Both interior and boundary formulas are presented. Although all of the optimized filters only maintain fourth-order accuracy, they have the characteristic of sharp spectral cutoff and do not contaminate the stability of the spatial discretization methods. A set of modified Gaussian functions are introduced in this paper. These functions possess a sharp cutoff. So it is reasonable to make the transfer functions of the filters approximated to the Gaussian functions. The advanced sequential quadratic programming (SQP) method [4] is employed to get the approximation.

The organization of the paper is as follows. Section 2 gives a brief introduction of the high-accuracy and maximum-resolution (HAMR) compact finite difference schemes [4] and analyses their behavior using dispersive wave theory. Section 3 describes the main strategies and shows a detailed procedure to optimize the filters. The improved performances of the optimized filters are exhibited when applied to one- and two-dimensional problems in Section 4. And conclusions are made in Section 5.

2. HAMR COMPACT FINITE DIFFERENCE SCHEMES

The HAMR compact finite difference schemes of [4] are the optimization of generalized Padé schemes [2]. They can be expressed as

$$\begin{aligned}&\beta f'_{i-2}+\alpha f'_{i-1}+f'_i+\alpha f'_{i+1}+\beta f'_{i+2}\\&\quad=a\frac{f_{i+1}-f_{i-1}}{2\Delta x}+b\frac{f_{i+2}-f_{i-2}}{4\Delta x}+c\frac{f_{i+3}-f_{i-3}}{6\Delta x}\quad \text{for } i=3,\ldots,N-3\end{aligned}\tag{1}$$

DOI: 10.1002/fld

$$\left.\begin{aligned} \sum_{m=0}^{4} a_{im} f'_i &= \frac{1}{\Delta x} \sum_{n=0\neq i}^{6} p_{in}(f_n - f_i) \\ \sum_{m=0}^{4} a_{im} f'_{N-m} &= -\frac{1}{\Delta x} \sum_{n=0\neq i}^{6} p_{in}(f_{N-n} - f_{N-i}) \end{aligned}\right\} \quad \text{for } i = 0, 1, 2 \tag{2}$$

where Equation (1) is the interior scheme and Equation (2) is the numerical boundary scheme. The interior scheme keeps fourth-order Taylor accuracy and the boundary filters possess third-order accuracy. All of them have the characteristics of low-dispersion and low-dissipation. What is more important is that the whole scheme is asymptotically stable. The well-resolved wave number-domain of HAMR schemes range from 0 to nearly 0.8π and the real part of modified scaled wave numbers are illustrated in Figure 1.

Numerical dispersion is the result of the variation of the group velocity (GV) of a numerical scheme. In order to keep low-dispersion, the GV of the spatial discretization should be equal to one under specific tolerance, for example, 0.02. The GV of HAMR schemes are shown in Figures 2 and 3. During the computation, the deviation between GV and one will introduce spurious waves, which include dispersive waves (positive GV) and parasite waves (negative GV). From Figure 2 we can see that the parasite waves have very large wave numbers and they are responsible for the often observed grid-to-grid oscillations [5, 19]. The spurious waves, especially the parasite waves, must be damped as soon as they are generated to keep the stability of the computation. And filters are one of the best choices to suppress the spurious without affecting the well-resolved long waves.

3. OPTIMIZED COMPACT FILTERING SCHEMES

3.1. Interior filtering schemes

Most of the compact filters commonly used [7–18] in the DNS and LDS are on the basis of [2]. The coefficients of these filters are derived by matching the Taylor series coefficients of various

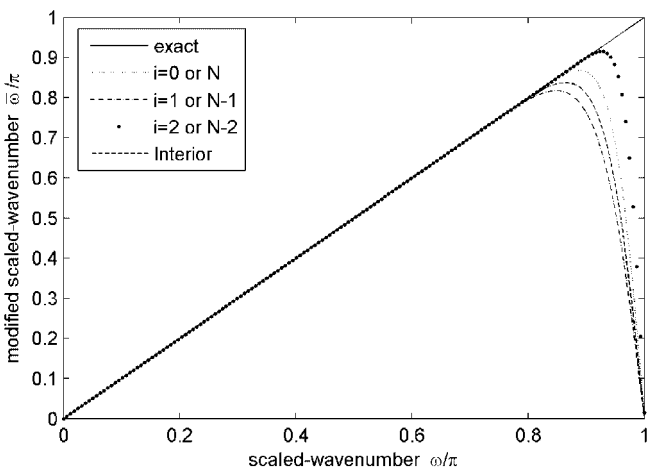

Figure 1. Real part of modified scaled-wave numbers of HAMR schemes.

DOI: 10.1002/fld

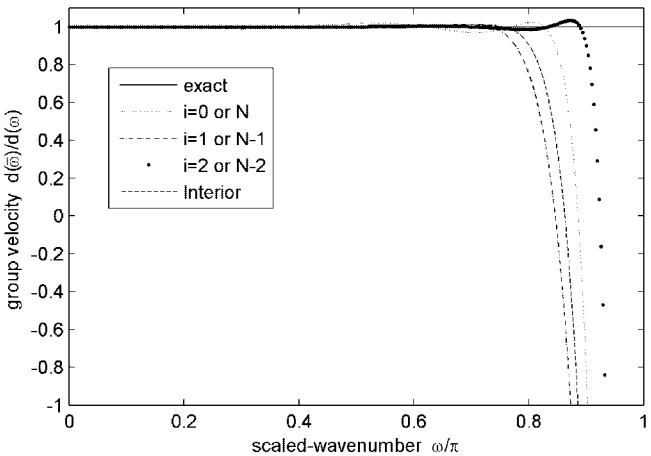

Figure 2. The group velocity of HAMR schemes.

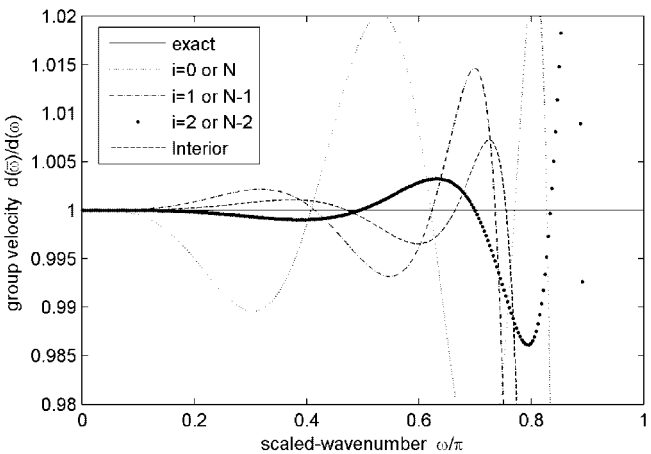

Figure 3. Enlarged graph of Figure 2.

orders. But the higher-order filters, for example, 10th order in [14], only ensure less impact on well-resolved waves and cannot guarantee a sharp spectral cutoff. And the high-order filters usually are large stencils, for example, 10th-order filters of [10] need 11 points. The interior filters considered here are pentadiagonal symmetric schemes, which are expressed as

$$\beta\hat{f}_{i-2}+\alpha\hat{f}_{i-1}+\hat{f}_i+\alpha\hat{f}_{i+1}+\beta\hat{f}_{i+2}=\sum_{l=0}^{n}\frac{p_l}{2}(f_{i+l}+f_{i-l}) \tag{3}$$

where $\hat{f}_i$ denotes the filtered variable at grid point i. A series of $2n+1$ points stencil filters can be obtained from Equation (3). The tridiagonal filters of [10] can also be expressed in Equation (3) when β is set equal to 0. And α is their control variable, which is usually ranged from 0 to 0.5. For convenient reference in the following, the filter of [10] is called standard filters and denoted

DOI: 10.1002/fld

as stdO$N\alpha x$, where N is the order of the filter and x is the value of control variable α. Through Fourier analysis, the transfer functions (TF) of the above filters are derived as

$$\mathrm{TF}(\omega)=\frac{\sum_{l=0}^{n} p_l \cos(l\omega)}{1+2\alpha\cos(\omega)+2\beta\cos(2\omega)} \tag{4}$$

where ω is the modified wave number. The optimization is to obtain the coefficients of Equation (3) to guarantee that the transfer functions have a sharp spectral cutoff—completely attenuate grid-to-grid oscillations but leave the well-resolved waves undisturbed. So a modified Gaussian function is introduced and defined as

$$\mathrm{GF}(\omega)=1-\exp\left[-\ln(2)\left(\frac{\omega-\pi}{\sigma}\right)^2\right] \tag{5}$$

The modified Gaussian function defined in Equation (5) has all the characteristics that the filters require, and different filters can be derived with different half-width σ. Therefore, what we should do is to let $\mathrm{TF}(\omega)$ approximate to $\mathrm{GF}(\omega)$ over the range $\omega\in[0, 0.80\pi]$, which is the well-resolved domain of HAMR schemes [4]. And the coefficients of the filters can be derived by minimizing the integral

$$\int_0^{0.8\pi}[\mathrm{TF}(\omega)-\mathrm{GF}]^2 d_\omega \tag{6}$$

Obviously, the integral is a nonlinear function of the coefficients. And during the optimization, the following constrains must be satisfied

(1) $\mathrm{TF}(\pi)=0$, to completely damp grid-to-grid oscillations;
(2) $\mathrm{TF}(0)=1$, to leave the infinitely long waves not attenuated at all;
(3) nth-order Taylor accuracy (be referred to as On) for $n+3$ point stencil filters, to leave the long waves undisturbed;
(4) $\forall\omega\in[0,1]:|\mathrm{TF}(\omega)|\leqslant 1$, not to amplify any waves and to keep the stability of the filter.

Now the objective is reduced to find the minimum of a multi-variable function with multi-constraint. We can obtain the coefficients by SQP method [4]. In order to keep the well-resolved waves undisturbed by the filters, the filters we optimized have at least fourth-order Taylor accuracy. During the application we find that the high-order filters ($n>4$) do not perform better than the lower ones ($n=4$), which will be explained in detail in Section 4. So the high-order filters presented here only include 6- and 8-order with $\sigma=0.15\pi$ (denoted as op$O6\sigma0.15\pi$ and op$O8\sigma0.15\pi$, the same below). The optimized fourth-order filters presented here only contain $\sigma=0.10\pi, 0.15\pi$ and 0.20π. And they are adequate for different computation requirements. All of the coefficients of the optimized filters mentioned above are presented in Table I. And the transfer functions of the optimized filters are shown in Figures 4–7, compared with the 10th-order standard tridiagonal filters with different control variables α.

From Figure 4 we can see that all of the optimized filters in the figure approximate to the Gaussian function perfectly. No matter what the value of the control variable is, the standard 10th-order tridiagonal filter cannot possess the cutoff as sharp as the optimized filters. It can be seen from Figure 5 that the three optimized fourth-order filters can attenuate waves in different wave number domains. The filtering domain of the optimized filters covers the domain of standard filters with the control variable α ranging from 0.10 to 0.49. So the optimized three fourth-order

DOI: 10.1002/fld

Table I. Optimized coefficients of interior filters.

	$O4\sigma0.20\pi$	$O4\sigma0.15\pi$	$O4\sigma0.10\pi$	$O6\sigma0.15\pi$	$O8\sigma0.15\pi$
α	0.5673952755	0.6393918014	0.6598365353	0.6307212910	0.6192779275
β	0.1209216774	0.1503303266	0.1614814366	0.1452737099	0.1389919478
p_0	0.9665459988	0.9931634217	0.9989719367	0.9920416459	0.9902970056
p_1	1.1849715528	1.2890384701	1.3212151655	1.2741759485	1.2547275123
p_2	0.2217709541	0.2965587062	0.3223460352	0.2841807365	0.2687429486
p_3	0.0033454001	0.0006836578	0.0001028063	0.0018190524	0.0034653551
p_4	0	0	0	−0.0002273815	−0.0007700789
p_5	0	0	0	0	0.0000770079

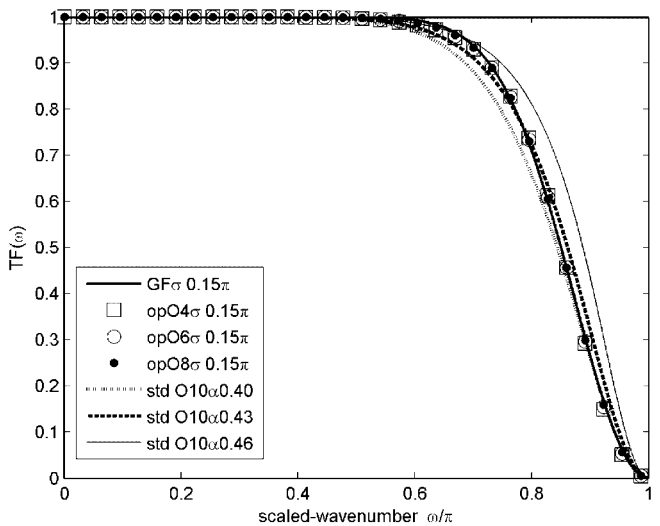

Figure 4. Transfer functions of optimized filters of different order with $\sigma=0.15\pi$.

filters are adequate for different damping requirements. And it is easier and more convenient to select a proper filter from 3 optimized fourth-order filters than to choose an appropriate control variable of the standard filters.

In order to demonstrate the computation accuracy for the long waves, the deviations between the optimized filters' transfer functions and 1 $(1-\mathrm{TF}(\omega))$ are plotted in Figures 6 and 7 in log scale. From Figure 6 one can see that the dissipation for long waves $(k\Delta x<0.5\pi)$ of all of the filters, both optimized and the standard, are negligible. The optimized higher-order filters are a bit less dissipative than the fourth-order ones for the long waves. However, the optimized 4-order filter is sufficiently accurate for computation and this will be explained in detail in Section 4. From Figure 7 one can see that different optimized filters have different dissipations in the long waves, and you can choose the best one to use according to the induced spurious waves. Sharp cutoffs of the modified Gaussian functions are also illustrated in the two figures, and it is reasonable to make the transfer functions approximated to these modified functions.

DOI: 10.1002/fld

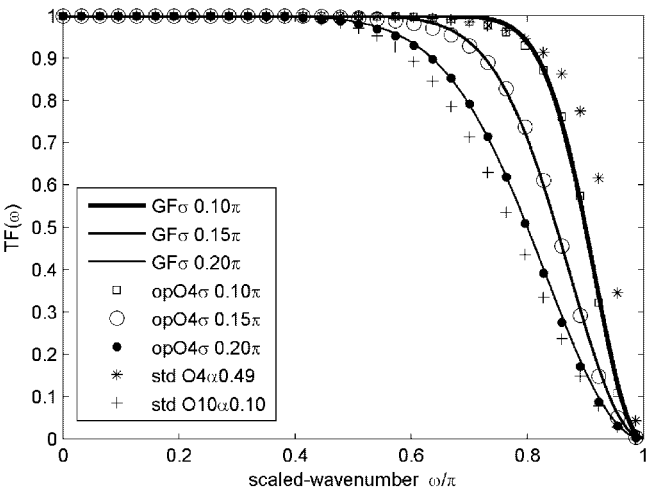

Figure 5. Transfer functions of optimized fourth-order filters with different half-width.

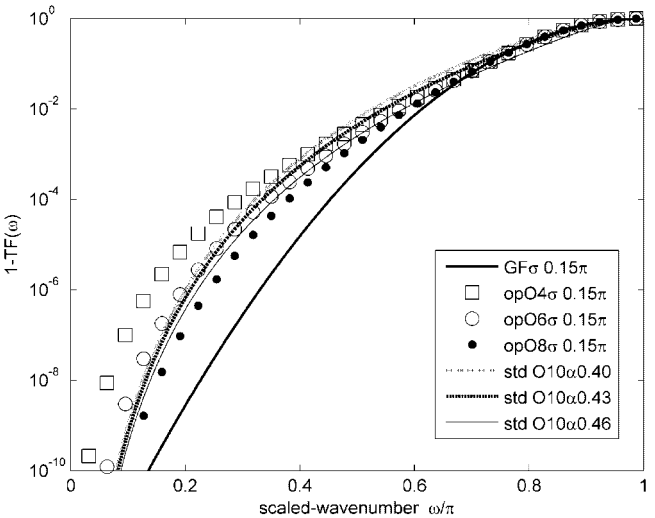

Figure 6. Transfer functions of filters in Figure 4 are plotted in log scale.

3.2. Near boundary filtering schemes

The interior filters are relatively large symmetric stencils and cannot be applied to boundary points directly, for example, the optimized fourth-order filters cannot be suitable at the boundary point $i = 1, 2$ and 3. There are two strategies for boundary filtering: the one is to lower the order of accuracy of the filters coupled if necessary with a corresponding increase in control variable α [10, 12], and the other is to exploit one-side high-order compact filters [7]. Generally, the standard lower-order filters may introduce excessive damping in the computation and contaminate the

DOI: 10.1002/fld

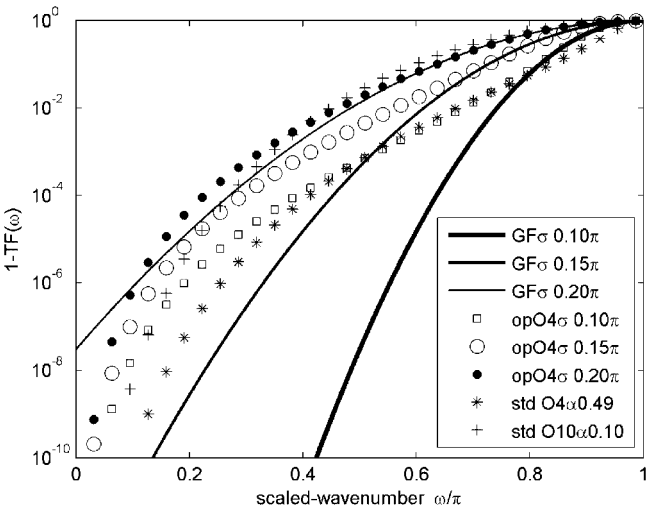

Figure 7. Transfer functions of filters in Figure 5 are plotted in log scale.

well-resolved long waves. And the one-side standard filters obtained in [7] cannot damp spurious waves in some scaled wave numbers no matter what the value of control variable α is.

The near boundary filters considered here are also one-side schemes, they are expressed as

$$\left.\begin{aligned} \sum_{m=1}^{5} a_{im}\hat{f}_i &= \sum_{n=1}^{6} b_{in} f_n \\ \sum_{m=1}^{5} a_{im}\hat{f}_{N+1-m} &= \sum_{n=1}^{6} b_{in} f_{N+1-n} \end{aligned}\right\} \quad \text{for } i=2,3 \tag{7}$$

where a_{ij} and b_{ij} are the coefficients to be optimized. In order to keep the system pentadiagonal, the coefficients, a_{22} and a_{33}, are set equal to one and a_{25} is set equal to zero. During the computation we find that the one-side filters at boundary point $i=1$ and N can greatly affect the stability of the computation. Therefore, no filters are applied at such two points in this paper. A lot of test cases have proved that this strategy has no impact on the accuracy of the computation.

Through Fourier analysis, the transfer function of the near boundary filters are given by

$$\mathrm{TF}(\omega)=\frac{\sum_{n=1}^{6} b_{in}\exp(I(n-1)\omega)}{\sum_{m=1}^{5} a_{im}\exp(I(m-1)\omega)} \quad \text{for } i=2,3 \tag{8}$$

where $I=\sqrt{-1}$. Obviously, the transfer function of Equation (8) is complex. In order to simplify TF at point $i=3$, we set $a_{21}=a_{25}$ and $a_{22}=a_{24}$. The real part of $\mathrm{TF}(\omega)$ should have sharp cutoff and it can also be obtained by approximating to the modified Gaussian function.

We can solve ω inversely from Equation (8) and obtain

$$\bar{\omega}=\varphi(\mathrm{TF}, A_i, B_i) \tag{9}$$

DOI: 10.1002/fld

Table II. Optimized coefficients of boundary filters.

	$i=2$			$i=3$		
	$\sigma 0.10\pi$	$\sigma 0.15\pi$	$\sigma 0.20\pi$	$\sigma 0.10\pi$	$\sigma 0.15\pi$	$\sigma 0.20\pi$
a_{i1}	0.3155721523	0.3096256995	0.3217547156	0.1604294991	0.1477868412	0.1346835856
a_{i2}	1	1	1	0.6588915457	0.6357553622	0.5779871517
a_{i3}	1.0733687821	1.1380646293	1.2703966806	1	1	1
a_{i4}	0.3807496437	0.4106696169	0.4689158656	0.6588915457	0.6357553622	0.5779871517
a_{i5}	0	0	0	0.1604294991	0.1477868412	0.1346835856
b_{i1}	0.3153161745	0.3084688023	0.3179036053	0.1603333770	0.1470348738	0.1311400585
b_{i2}	1.0012798892	1.0057844862	1.0192555517	0.6593721561	0.6395151994	0.5957047873
b_{i3}	1.0708090038	1.1264956568	1.2318855773	0.9990387791	0.9924803256	0.9645647288
b_{i4}	0.3833094221	0.4222385894	0.5074269689	0.6598527666	0.6432750366	0.6134224229
b_{i5}	−0.0012798892	−0.0057844862	−0.0192555517	0.1599488887	0.1440270040	0.1169659500
b_{i6}	0.0002559778	0.0011568972	0.0038511103	0.0000961221	0.0007519674	0.0035435271

Here A_i and B_i are coefficients vectors of a_{ij} and b_{ij} at boundary point i, and $\overline{\omega}$ is the modified scaled wave number. TF(ω) is a complex number, and $\overline{\omega}$ is also a complex number. During the computation, the imaginary part of $\overline{\omega}$ represents dissipative errors. It can be concluded from Equation (9) that the imaginary part of $\bar{\omega}$ comes from TF(ω). So the imaginary part of TF(ω) can cause dissipation as well as instability and should try to be approximated to zero. Therefore, we can derive the coefficients by minimizing the integral

$$\int_0^r \{[\mathrm{Re}(\mathrm{TF}(\omega)) - \mathrm{GF}]^2 + [\mathrm{Im}(\mathrm{TF}(\omega))]^2\} d_\omega \tag{10}$$

where r is the integral upper limit and is set equal to the corresponding maximum-scaled-wave number of HAMR boundary schemes. It is the same as interior schemes that the four constraints should be satisfied: (1) TF(π) = 0, (2) TF(0) = 1, (3) fourth-order Taylor accuracy, (4) $\forall \omega \in (0, 1)$: $|\mathrm{Re}(\mathrm{TF}(\omega))| \leqslant 1$. The SQP method is also employed to get the optimization. The optimized coefficients are presented in Table II.

The optimized boundary filters (denoted as opOneSideσx) are compared with the standard one-side filters in [7] (denoted as stdOneSideα, where α is the control variable) as well as lower-order symmetric filters in [10, 12]. The real parts of the filters are shown in Figures 8 and 9. And the imaginary parts of the filters are shown in Figures 8 and 9. We can see from Figures 8 and 9 that the real parts of the optimized filters at boundary points $i = 2$ and 3 fit the corresponding Gaussian functions very well. The standard one-side boundary filters amplify some short waves no matter what the value of the control variable is. The standard asymmetric filters at the boundary do not have so sharp spectral cutoff as the optimized ones. It can be seen from Figures 10 and 11 that the imaginary part of the optimized boundary filters approximate to zero very well in the wave number domain ranged from 0 to about 0.7π.

4. APPLICATION

In this section two problems are considered to investigate the performances of the optimized filters. The first problem involves the one-dimensional scalar wave convection and the second one

DOI: 10.1002/fld

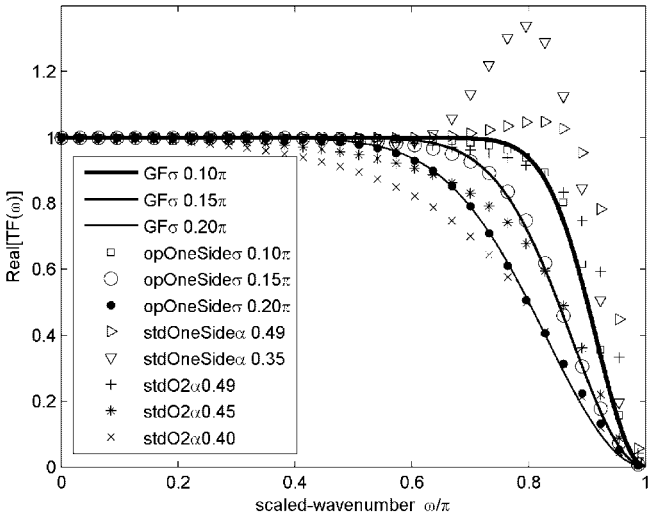

Figure 8. Real part of the transfer functions at boundary point $i=2$.

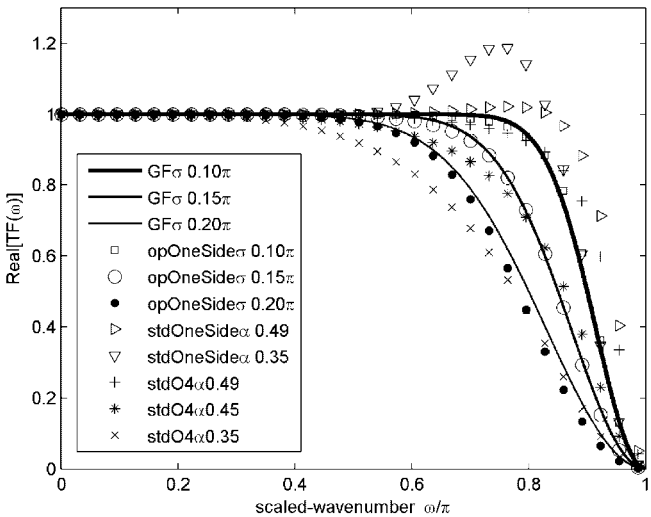

Figure 9. Real part of the transfer functions at boundary point $i=3$.

involves two-dimensional acoustic pulse convection. During the computation, HAMR schemes are employed to spatial discretization and five-stage LDDRK optimized scheme of Hu *et al.* [20] is applied to temporal integration. Both of the problems are unstable if filters are not used in the computation. The solutions obtained by optimized filters are compared with those of standard 10th-order ones under the same condition, namely the same boundary condition, the same difference schemes and the same time integration methods. Because the one-side standard formulas cannot

DOI: 10.1002/fld

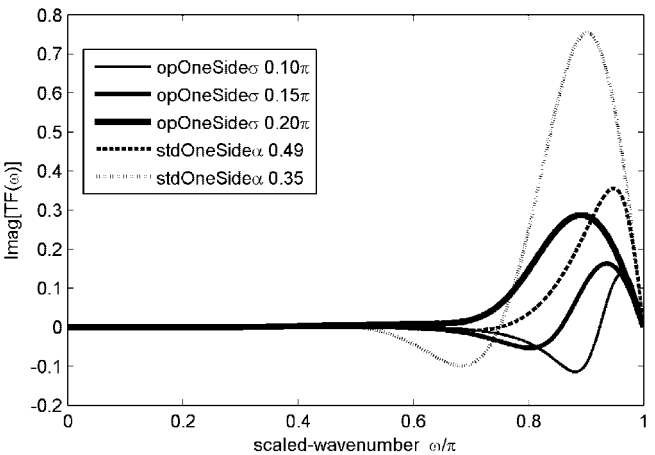

Figure 10. Imaginary part of the transfer functions at boundary point $i=2$.

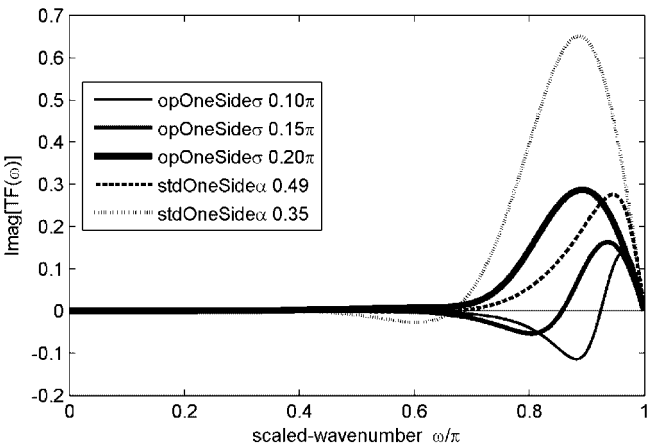

Figure 11. Imaginary part of the transfer functions at boundary point $i=3$.

satisfy the condition that does not amplify any waves, the lower-order symmetric formulas are employed to incorporate the standard interior schemes.

4.1. Problem I

The one-dimensional scalar wave convection is chosen as the first problem. The problem simulates the convection of an initial wave pulse and its transmission. It involves the simple convective wave equation which is expressed as

$$\frac{\partial u}{\partial t}+\frac{\partial u}{\partial x}=0 \tag{11}$$

DOI: 10.1002/fld

A trapeziform pulse

$$u(x,0)=\begin{cases} x-20, & x\in[20,30] \\ 10, & x\in(30,40) \\ -x+50, & x\in[40,50] \\ 0 & \text{others} \end{cases} \tag{12}$$

is designed as the initial condition. Equation (11) is solved on a uniform mesh employing four different spatial intervals ($\Delta x=0.5, 1, 2, 4$). The computation is done over the domain $x\in[1, 100]$. A small CFL number 0.1 is adopted to decrease the numerical errors induced by temporal integration. In order to give a stable solution, different filters are used to damp the spurious waves of u after the final stage of the 5-stage LDDRK.

Which filters to be used depends on the spurious waves generated in the computation. If the spurious waves are mostly located in the high scaled wave numbers (for example, $0.8\pi<k\Delta x\leqslant\pi$), all of the optimized filters can be used and different accuracies can be obtained. If the scaled wave numbers of the spurious waves possess a broad range (for example, $0.6\pi<k\Delta x\leqslant\pi$), the optimized filter with small width (for example, 0.10π) may be inappropriate to be used, for in such a case the filter cannot damp the spurious completely. The wave numbers of the spurious waves can be obtained from Fourier Transform, which is demonstrated in detail in Reference [5]. In practice, one should not use Fourier Transform but try with different filters. In uniform computation grid, at most 3 times may be tried if optimized filters are adopted. If use standard 10th-order filters, however, one must try many times to find the best combination of the five control variables (one for interior filter and four for boundary filters). It is laborious to adjust the 5 variables for standard filters. Therefore, the optimized filters are more convenient to be used.

During the computation, we find that all of the optimized filters are stable for the four different Δx, except op$O4\sigma0.10\pi$ with $\Delta x=0.5$. As explained in the previous paragraph, this is because the op$O4\sigma0.10\pi$ filter cannot damp the spurious waves exhaustively under this condition. So the

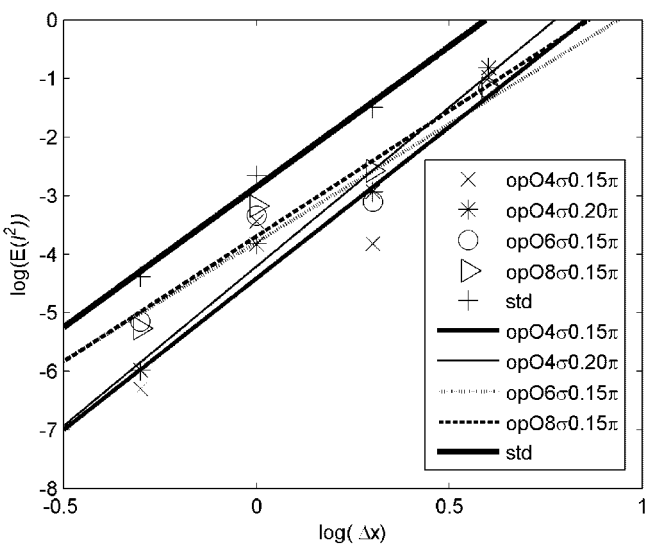

Figure 12. The l^2-norm error comparison of problem I.

DOI: 10.1002/fld

op$O4\sigma0.10\pi$ filter is not compared with the others in this problem. When standard filters are employed, many trials may be needed to choose a suitable control variable to keep the solution stable. But no matter what the control variable is, the solution is divergent when $\Delta x=4$. This is also because the damping domain of the 10th-order filter is not compatible with the wave number domain of spurious waves. In this example, the stable solution can be obtained when a filter with a wider damping domain, for example, eighth-order standard filter is used.

A systematic comparison of the filters is provided in Figure 12, which shows the l^2 norm errors (defined as $E(l^2)=\sqrt{\sum_{i=1}^{N}[f_{\text{num}}(i)-f_{\text{exact}}(i)]^2/N}$, where $f_{\text{num}}(i)$ stands for the numerical result at point i) of the results at $t=40$. In addition to the actual data points, linear least-square fits to the data are constructed to provide an estimate of the accuracy of the computation.

From Figure 12 we can see that the norm errors $E(l^2)$ of the optimized filters are smaller than those of the standard filters under the same spatial intervals. We can also see that the optimized fourth-order filters perform better than the higher-order ones especially when $\Delta x=0.5$. That is because many factors such as the spatial discretization schemes, the temporal integration methods, and the boundary conditions can affect the wave number range of spurious waves. The spatial discretization scheme applied in this paper is the HAMR scheme whose interior formula only possesses fourth-order formal accuracy. From Figure 3 we can see that in the well-resolved domain (range from 0.2π to about 0.8π) of the HAMR scheme, there exists minute dispersion. If there are a mass of computation steps, for example, longtime integration or small spatial interval, such minute dispersion may be cumulated and they should be removed. It is shown in Figure 6 that the optimized fourth-order filter can attenuate the minute dispersion more than the optimized higher-order ones. The optimized filters with different orders and widths may perform differently according to the spurious waves. But we can see that generally the optimized higher-order filters do not perform better than the fourth-order ones with the same width of Gaussian function. So only the results of op$O4\sigma0.15\pi$ are further compared with those of the standard filters when $\Delta x=1$ and 2. And they are shown in Figures 13 and 14. It can be seen from Figure 13 that both filters perform well. From Figure 14 we can see that when $\Delta x=2$, the standard filters cannot damp the spurious effectively as it does at $\Delta x=1$, however, the op$O4\sigma0.15\pi$ filter performs well.

4.2. Problem II

The second problem is to simulate the reflection of an acoustic pulse by a solid wall. The computation is done over the domain $x\in[-50,50]$ and $y\in[0,110]$. There is an initial pressure pulse released at $(0,15)$ and an acoustic pulse is generated. The wave front of the acoustic pulse expands radially. But a solid wall is located at $y=0$ and the acoustic pulse will be reflected. It involves the two-dimensional linearized Euler equation in the form of

$$\frac{\partial U}{\partial t}+\frac{\partial E}{\partial x}+\frac{\partial F}{\partial y}=0 \tag{13}$$

where

$$U=\begin{pmatrix}\rho\\ u\\ v\\ p\end{pmatrix},\quad E=\begin{pmatrix}M_x\rho+u\\ M_x u+p\\ M_x v\\ M_x p+u\end{pmatrix},\quad F=\begin{pmatrix}M_y\rho+v\\ M_y u\\ M_y v+p\\ M_y p+v\end{pmatrix} \tag{14}$$

DOI: 10.1002/fld

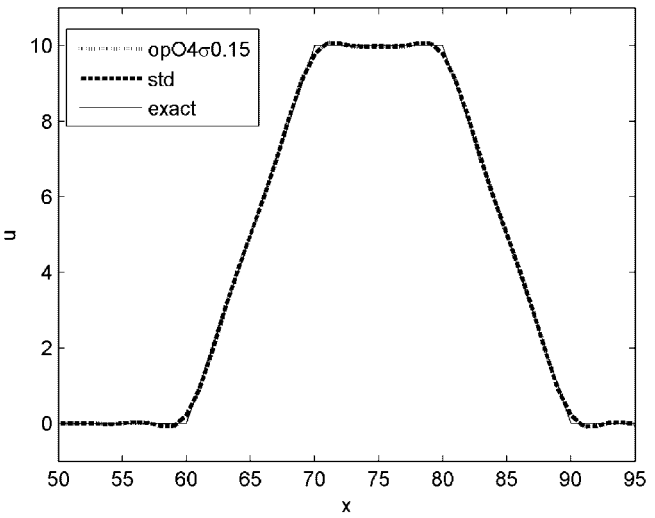

Figure 13. The results comparison of problem I with $\Delta x = 1$ at time $t = 40$.

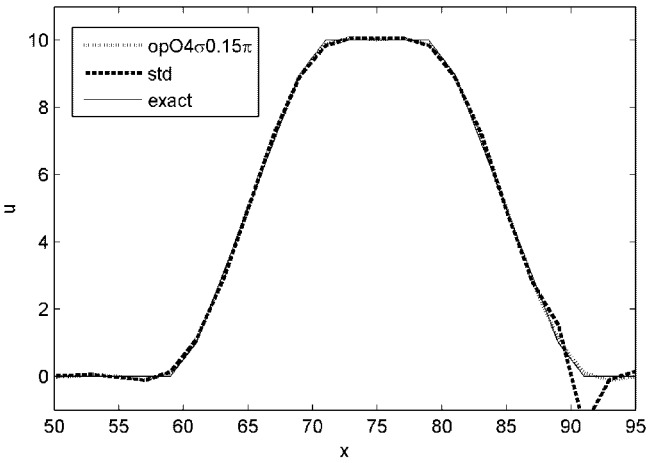

Figure 14. The results comparison of problem I with $\Delta x = 2$ at time $t = 40$.

In the above, ρ, u, v and p are the density, velocities and pressure, respectively. M_x an M_y are the Mach numbers of the mean flow in the x and y directions and both of them are set equal to 0 in the computation. And all the variables are non-dimensionalized. The initial conditions are given as

$$\begin{aligned} u &= v = 0 \\ p &= \rho = \varepsilon \exp\left\{-(\ln 2)\frac{x^2 + (y-15)^2}{9}\right\} \end{aligned} \tag{15}$$

DOI: 10.1002/fld

The simulation is done over a domain with four different uniform grids ($\Delta x = \Delta y = 0.5, 1, 2, 4$) and ε is set equal to 0.01. CFL number of 0.2 is employed. During the simulation, perfectly matched layers (PML) of 10 grid points are applied to absorbing out-going waves at left, right and upper of computation domain [21]. Wall boundary $v = 0$ is applied at the lower of the domain [22]. In order to keep the solution stable, different filters are used to damp the spurious waves of the four variable of U after the final stage of the 5-stage LDDRK. Each time the filter is first applied at the x direction and then at the y direction.

During the computation we find that all of the optimized filters can keep the solution stable no matter what the spatial intervals are. However, many trials are required for the standard filters to obtain a stable solution. Both the interior and the boundary formulas have the impact on the stability of the solution. It is time-consuming and laborious to select the control variables of the standard schemes. The control variables of the standard filters employed in this problem are 0.35 for interior formula and 0.30 for the boundary schemes.

For a systematic comparison, the l^2 norm errors of different filters at time $t = 80$ are compared in Figure 15. And the l^2 error is defined as

$$E(l^2) = \sqrt{\frac{\sum_{i=1}^{Nx} \sum_{j=1}^{Ny} [p_{\text{num}}(i, j) - p_{\text{exact}}(i, j)]^2}{NxNy}} \tag{16}$$

From Figure 15(a) we can see that no matter what the spatial intervals are, the errors of the optimized filters are less than the standard ones. And the high-order optimized filters do not perform better than the fourth-order optimized schemes. From Figure 15(b) we can see that there is nearly no difference of the three optimized fourth-order filters when $\Delta x = 1$ and 2. Because the damping domain of the op$O4\sigma 0.20\pi$ filter is larger than the other two filters, the numerical error of the op$O4\sigma 0.20\pi$ filter is bigger than the others when $\Delta x = 0.5$ and 4, for excessive damping may be introduced.

The solutions of the op$O4\sigma 0.15\pi$ and standard filters are further compared. Their pressure contours at $t = 40$ with $\Delta x = 2$ (a relative coarse grid) are provided in Figures 16 and 17. From the figures we can see that the contour lines of op$O4\sigma 0.15\pi$ are more smooth than those of the

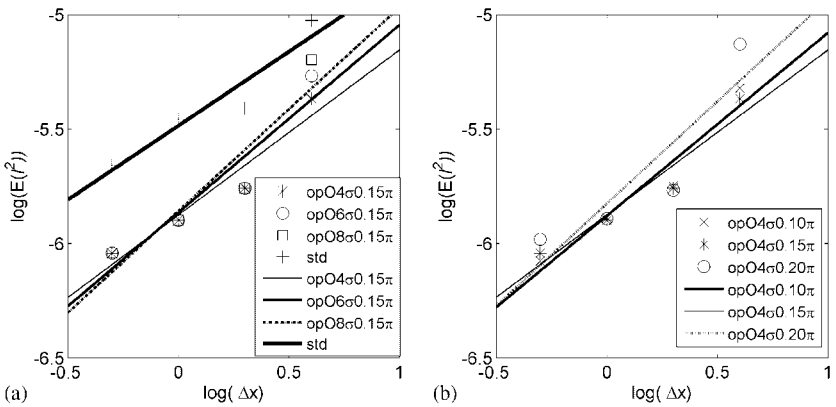

Figure 15. The l^2-norm error comparison of problem II.

DOI: 10.1002/fld

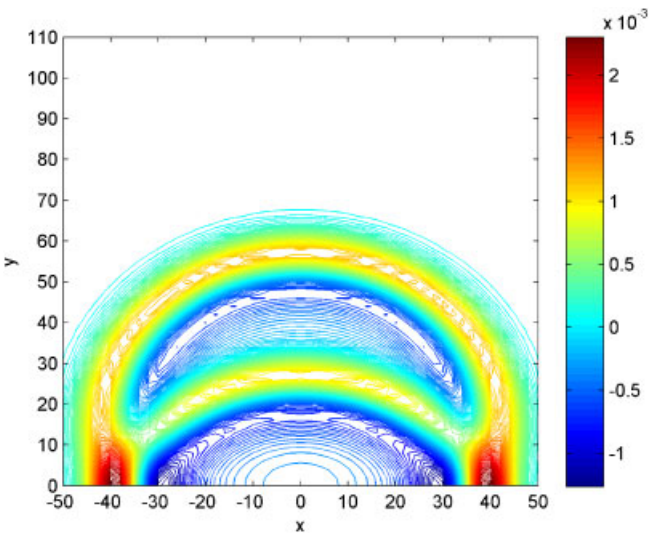

Figure 16. Pressure contour at time $t=40$ (op$O4\sigma 0.15\pi$ filter, $\Delta x=2$).

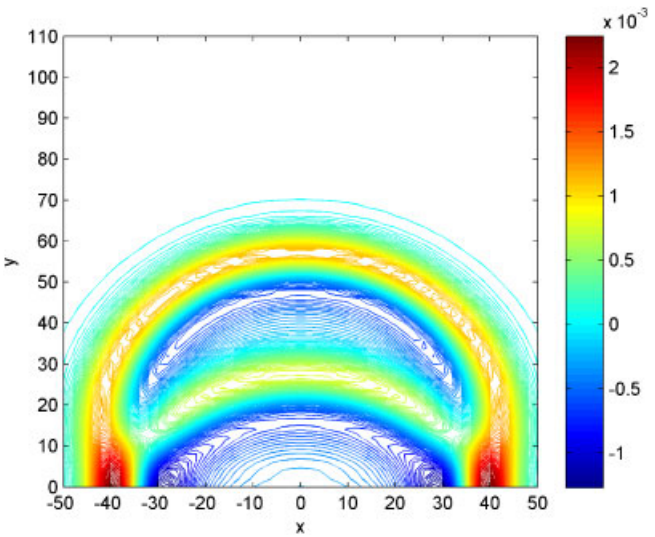

Figure 17. Pressure contour at $t=40$ (standard filter, $\Delta x=2$).

standard filters. The pressure waveform along the axis of $x=0$ at $t=40$ are compared in Figure 18. It can be seen that the waveform of the filter op$O4\sigma 0.15\pi$ approximates to the exact curve very well, however, there is relative bigger deviation of the waveform between the standard filters and exact. The same conclusion can be made at $t=80$, and the pressure contours and waveforms are presented in Figures 19–21.

DOI: 10.1002/fld

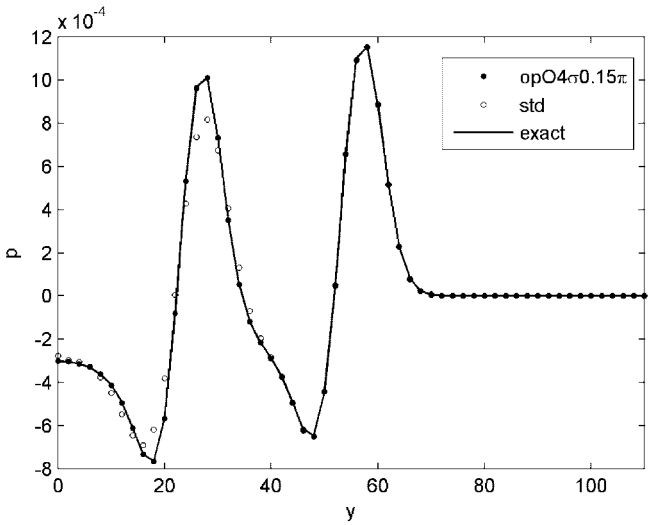

Figure 18. Pressure waveform along the axis of $x=0$ at time $t=40$.

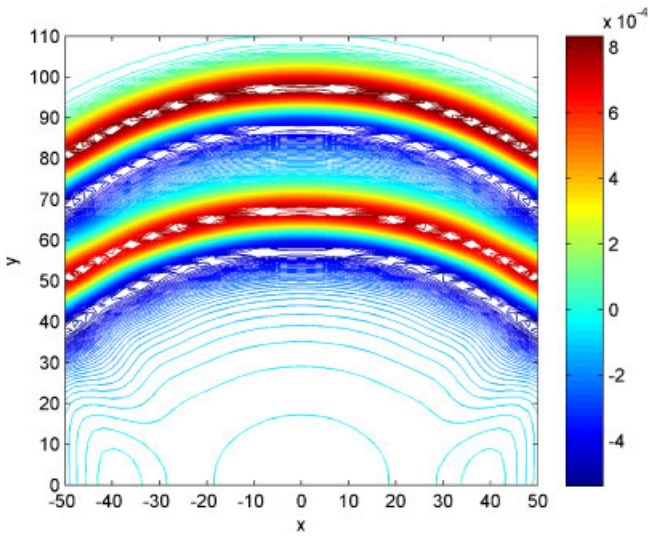

Figure 19. Pressure contour at time $t=80$ (op$O4\sigma0.15\pi$ filter, $\Delta x=2$).

5. CONCLUSION

The pentadiagonal filtering schemes are optimized in this paper. All of the optimized filters have sharp spectral cutoff which damp the high-wave number spurious waves but leave the well-resolved waves unaffected. Both the interior and boundary optimized filters have good stability. The optimized high-order filters do not perform better than the optimized fourth-order filters when

DOI: 10.1002/fld

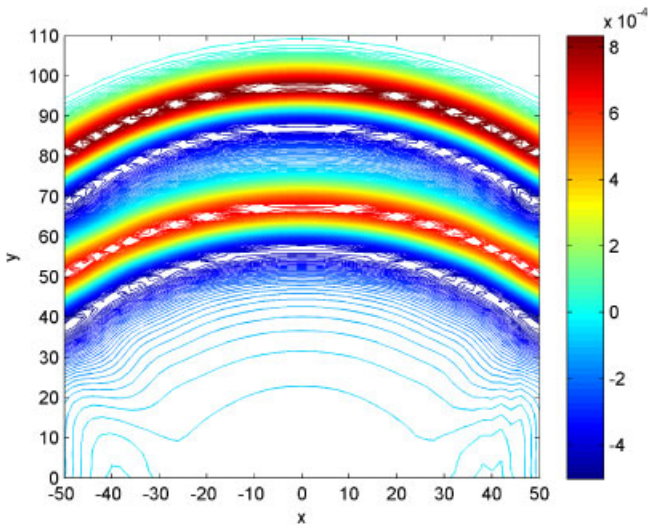

Figure 20. Pressure contour at time $t = 80$ (standard filter, $\Delta x = 2$).

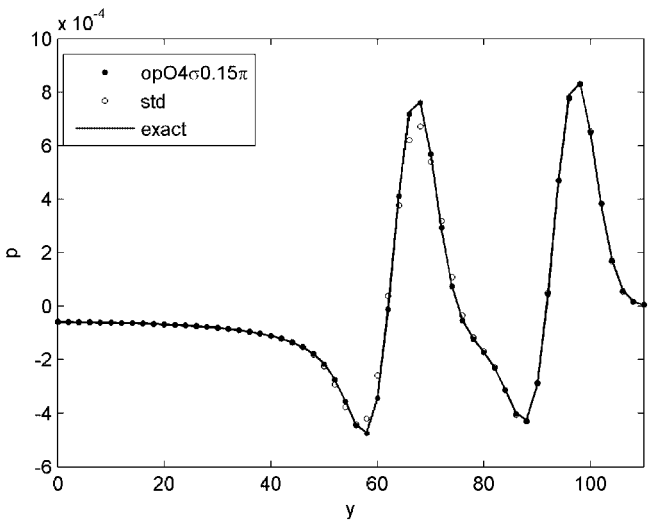

Figure 21. Pressure waveform along the axis of $x = 0$ at time $t = 80$.

compared in the actual application. The optimized fourth-order filters are 7-point stencils which are smaller than the standard 10th-order filters. They are sufficient for different kinds of requirements. In the computation where a filter is required, what you need do is to select a proper one from the optimized fourth-order filters on the basis of the wave number domain of the spurious. And this is much easier and more convenient than to choose a suitable standard filter by adjusting its control

DOI: 10.1002/fld

variable. The improved performances of the optimized filters are demonstrated when applying in both one and two-dimensional test problems.

ACKNOWLEDGEMENTS

Project (No. 50075029) supported by the National Natural Science Foundation of China.

REFERENCES

1. Tam CKW, Webb JC. Dispersion-relation-preserving finite difference schemes for computational acoustics. *Journal of Computational Physics* 1993; **107**:262–281.
2. Lele SK. Compact finite difference schemes with spectral-like resolution. *Journal of Computational Physics* 1992; **103**:16–42.
3. Kim JW. Optimized boundary compact finite difference schemes for computational aeroacoustics. *Journal of Computational Physics* 2007; **225**:995–1019.
4. Liu ZX, Huang QB, Zhao ZG, Yuan JX. Optimized compact finite difference schemes with high accuracy and maximum resolution. *International Journal of Aeroacoustics* 2008; **7**(2):123–146.
5. Tam CKW, Webb JC. A study of the short wave components in computational acoustics. *Journal of Computational Acoustics* 1993; **1**:1–30.
6. Colonius T, Lele SK. Computational aeroacoustics: progress on nonlinear problems of sound generation. *Progress in Aerospace Sciences* 2004; **40**:345–416.
7. Gaitonde DV, Visbal MR. Further development of a Navier–Stokes solution procedure based on higher-order formulas. *AIAA Paper 99-0577*, 1999.
8. Vichnevetsky R. Numerical filtering for partial differential equations. *Technical Report NAM 156*, Rutgers University, 1974.
9. Alpert P. Implicit filtering in conjunction with explicit filtering. *Journal of Computational Physics* 1981; **44**: 212–219.
10. Gaitonde DV, Younge JL. Practical aspects of high-order accurate finite-volume schemes for electromagnetics. *AIAA Paper 97-0363*, 1997.
11. Visbal MR, Gaitonde DV. High-order accurate methods for unsteady vertical flows on curvilinear meshes. *AIAA Paper 98-0131*, 1998.
12. Visbal MR, Gaitonde DV. High-order accurate methods for complex unsteady subsonic flows. *AIAA Journal* 1999; **37**:1231–1239.
13. Visbal MR, Gaitonde DV. Computation of aeroacoustic field on general geometries using compact differencing and filtering schemes. *AIAA Paper 99-3706*, 1999.
14. Gaitonde DV, Visbal MR. Further development of a Navier–Stokes solution procedure based on high-order formulas. *AIAA Paper 99-0557*, 1999.
15. Visbal MR, Gaitonde DV. On the use of higher-order finite-difference schemes on curvilinear and deforming meshes. *Journal of Computational Physics* 2002; **181**:155–185.
16. Koutsavdis EK, Blaisdell GA, Lyrintzis AS. On the use of compact schemes with spatial filtering in computational aeroacoustics. *AIAA Paper 99-0360*, 1999.
17. Rizzetta DP, Visbal MR, Blaisdell GA. Application of high-order compact difference scheme to large-eddy and direct numerical simulation. *AIAA Paper 99-3714*, 1999.
18. Visbal MR, Rizzetta DP. Large-eddy simulation on general geometries using compact differencing and filtering schemes. *AIAA Paper 2002-0288*, 2002.
19. Bogey C, Bailly C. A family of low dispersive and low dissipative explicit schemes for flow and noise computations. *Journal of Computational Physics* 2004; **194**:194–214.
20. Hu FQ, Hussaini MY, Manthe JL. Low-dissipation and low-dispersion Runge–Kutta schemes for computational acoustics. *Journal of Computational Physics* 1996; **124**:177–191.
21. Hu FQ. On absorbing boundary conditions for linearized Euler equations by a perfectly matched layer. *Journal of Computational Physics* 1996; **129**:201–219.
22. Edgar NB. A study of the accuracy and stability of high-order compact difference methods for computational aeroacoustics. *Ph.D. Dissertation*, University of Kansas, U.S.A., 2001.

DOI: 10.1002/fld